

Eigenspectrum, Chern Numbers and Phase Diagrams of Ultracold Color-orbit Coupled SU(3) Fermions in Optical Lattices

Man Hon Yau and C. A. R. Sá de Melo

School of Physics, Georgia Institute of Technology, Atlanta, 30332, USA

(Dated: November 26, 2021)

We study ultracold color fermions with three internal states Red, Green and Blue with SU(3) symmetry in optical lattices, when color-orbit coupling and color-flip fields are present. This system corresponds to a generalization of two-internal state fermions with SU(2) symmetry in the presence of spin-orbit coupling and spin-flipping Zeeman fields. We investigate the eigenspectrum and Chern numbers to describe different topological phases that emerge in the phase diagrams of color-orbit coupled fermions in optical lattices. We obtain the phases as a function of artificial magnetic, color-orbit and color-flip fields that can be independently controlled. For fixed artificial magnetic flux ratio, we identify topological quantum phases and phase transitions in the phase diagrams of chemical potential versus color-flip fields or color-orbit coupling, where the chirality and number of midgap edge states changes. The topologically non-trivial phases are classified in three groups: the first group has total non-zero chirality and exhibit only the quantum charge Hall effect; the second group has total non-zero chirality and exhibit both quantum charge and quantum color Hall effects; and the third group has total zero chirality, but exhibit the quantum color Hall effect. These phases are generalizations of the quantum Hall and quantum spin Hall phases for charged spin-1/2 fermions. Lastly, we also describe the color density of states and a staircase structure in the total and color filling factors versus chemical potential for fixed color-orbit, color-flip and magnetic flux ratio. We show the existence of incompressible states at rational filling factors precisely given by a gap-labelling theorem that relates the filling factors to the magnetic flux ratio and topological quantum numbers.

I. INTRODUCTION

Ultracold fermions loaded in optical lattices have become ideal systems to study related electronic phase diagrams and transport properties, because they provide a clean and well controlled playground to change various lattice parameters and external fields at the turn of a knob. While several experimental groups have worked mostly with Fermi isotopes ^6Li and ^{40}K using two internal states to study various aspects of interacting SU(2) fermions, there has been a growing interest in studying SU(N) generalizations of these systems. Examples of atomic SU(N) fermions found in nature are fermionic isotopes of closed shell atoms with two electrons in their outer electronic configuration. Two systems have been studied by several groups, one of them is ^{173}Yb , a fermionic isotope of Ytterbium and the other is ^{87}Sr , a fermionic isotope of Strontium.

The fermionic isotope ^{173}Yb has electronic shell structure $[\text{Xe}]4f^{14}6s^2$, with electronic spin $S = 0$ and nuclear spin $I = 5/2$. The electronic ground state of ^{173}Yb is $^1\text{S}_0$, which is six-fold degenerate because of its nuclear spin. The six degenerate states have nuclear spin projections $m_I = \{\pm 5/2, \pm 3/2, \pm 1/2\}$. Atoms in any selected state can be manipulated out of a trap or transformed into a desired nuclear spin state, so that the ground state of trapped ^{173}Yb can be up to six-fold degenerate [1–6].

The fermionic isotope ^{87}Sr has electronic shell structure $[\text{Kr}]5s^2$, with electronic spin $S = 0$ and nuclear spin $I = 9/2$. The electronic ground state of ^{87}Sr is $^1\text{S}_0$, which is ten-fold degenerate because of its nuclear spin. The ten degenerate states have nuclear spin pro-

jection $m_I = \{\pm 9/2, \pm 7/2, \pm 5/2, \pm 3/2, \pm 1/2\}$. Again, atoms in any selected state can be manipulated out of a trap or transformed into a desired nuclear spin state, so that the ground state of trapped ^{87}Sr can be up to ten-fold degenerate [7–11]. In addition, interactions between these close shell atoms are independent of their nuclear spin states at the atomic energy scales of interest, and therefore interactions are SU(N) symmetric. Since experiments are conducted at very low temperatures, the collisional properties of these atoms are dominated by s-wave scattering, and the interactions are local in space, that is, they are contact interactions described by a delta function potential that is independent of the nuclear spin states of the atoms. As a result, ^{173}Yb can be up to SU(6) symmetric, while ^{87}Sr can be up to SU(10) symmetric in their nuclear spin projections. In addition, orbital-Feshbach resonances can be used to control the strength of the SU(N)-symmetric interactions from weak to strong [12, 13]. Since any three nuclear states of ^{173}Yb or ^{87}Sr can be selected and trapped in an optical lattice, we label these nuclear states by color $\{R, G, B\}$ or pseudo-spin $\{\uparrow, 0, \downarrow\}$ to describe a Fermi system with SU(3) symmetry.

It is now possible to create artificial magnetic fields [14] in optical lattices [15, 16] that mimic electronic materials exhibiting integer [17] and fractional [18] quantum Hall effects. The synthetic magnetic flux values created are sufficiently large to allow for the experimental exploration of the intricacies of the Harper's model [19] and the Hofstadter butterfly [20], as well as the experimental determination of Chern numbers [21]. In addition, artificial magnetic fields for SU(2) fermions in optical lattices

could be used to simulate the phenomenon of magnetic field induced reentrant superfluidity, as discussed in the context of superconductivity in condensed matter physics for spin-1/2 fermions in standard lattices [22–25]. Furthermore, the creation of artificial spin-orbit coupling for ultra-cold atoms [26] also allows for the simulation of electronic materials exhibiting the quantum spin-Hall effect [27–29].

For ultracold fermions in optical lattices, artificial magnetic fields enable studies of topological insulators that break time reversal symmetry, such as quantum hall systems, while artificial spin-orbit fields allow for studies of topological insulators that do not break time reversal symmetry, such as quantum spin-Hall systems. Both types of topological insulators are characterized by Berry curvatures and Chern numbers, which have been measured experimentally using time of flight techniques [30], inspired by theoretical proposals [31, 32], and using dynamics of the center of mass of the atomic cloud [33], also motivated by theoretical work [34, 35]. However, studies of ultracold fermions may go beyond the quantum simulation of spin-1/2 topological insulators under typical condensed matter conditions [36], because artificial magnetic, spin-orbit and Zeeman fields may be adjusted independently [37].

Artificial magnetic, spin-orbit and Zeeman fields in spin-1/2 ultracold Fermi atoms may be independently tuned via a combination of experimental techniques that produce artificial magnetic fluxes without using internal states, such as laser assisted tunneling [15, 16], and that produce spin-orbit and Zeeman fields using internal states, such as Raman processes [26] or radio-frequency chips [38, 39]. These techniques can also be applied to SU(3) fermions with three internal states (colors) and allow for the investigation of exotic topological insulating phases that arise in optical lattices when artificial magnetic, color-orbit and color-flip fields are varied. The present system in optical lattices expands the realm of phases beyond Fermi liquid and superfluid for SU(3) fermions in the presence of color-orbit and color-flip fields analyzed in the continuum or in harmonic traps [40, 41].

In this manuscript, we study the interplay of artificial magnetic, color-orbit and color-flip fields for ultracold SU(3) fermions with three internal states (colors) and their effects on topological insulators in regimes that cannot be reached or found in condensed matter physics. We investigate the eigenspectrum and Chern numbers to describe different topological phases that emerge in the phase diagrams of color-orbit coupled fermions in optical lattices. We obtain the phases as a function of artificial magnetic, color-orbit and color-flip fields that can be independently controlled. For a fixed artificial magnetic flux ratio, we identify the topological quantum phases and phase transitions in the phase diagrams of chemical potential versus color-flip fields or color-orbit coupling, where the chirality and number of midgap edge states change. The topologically non-trivial phases are classified in three groups: the first group has total non-zero

chirality and exhibit only the quantum charge Hall effect; the second group has total non-zero chirality and exhibit both quantum charge and quantum color Hall effects; and the third group has total zero chirality, but exhibit the quantum color Hall effect. These phases are generalizations of the quantum Hall and quantum spin Hall phases for charged spin-1/2 fermions. Lastly, we also describe the color density of states and a staircase structure in the total and color filling factors versus chemical potential for fixed color-orbit, color-flip and magnetic flux ratio. We show the existence of incompressible states at rational filling factors precisely given by a gap-labelling theorem that relates the filling factors to the magnetic flux ratio and topological numbers.

The remainder of this manuscript is organized as follows. In Sec. II, we describe the three-color Hamiltonian for ultracold fermions loaded into a square optical lattice and in the presence of artificial magnetic, color-orbit and color-flip fields. In Sec. III, we analyze the energy spectrum obtained from a generalized Harper’s matrix with open boundary conditions and obtain the energy dispersions for bulk and edge states. In Sec. IV, we discuss the color Chern numbers to classify the insulating phases in the *charge* sector. We compute the Chern numbers via the Berry curvatures associated with the eigenstates of the Hamiltonian with periodic boundary conditions. We confirm the existence of a bulk-edge correspondence by comparing the Chern number calculated via periodic boundary conditions to the number of chiral edge states obtained via open boundary conditions. In Sec. V, we describe the phase diagrams of chemical potential versus color-flip field (Sec. V A), the gap labelling theorem (Sec. V B), and the phase diagrams of chemical potential versus color-orbit coupling (Sec. V C). We identify phases that exhibit quantum charge Hall and quantum color Hall effects in analogy to the quantum Hall effect and quantum spin Hall effect for spin-1/2 systems, and we find phases that exhibit simultaneously quantum charge and color Hall effect, which do not exist in spin-1/2 systems. In Sec. VI, we analyze the color density of states for the system with periodic boundary conditions, and show that the bulk gaps match precisely with the gaps obtained for open boundary conditions. Furthermore, we compute directly the filling factor as a function of the chemical potential and reveal the existence of filling factor steps at the precise values given by the gap-labelling theorem discussed in Sec. V B to describe insulating states. Finally, in Sec. VII, we summarize our results and state our conclusions.

II. THREE-COLOR HAMILTONIAN

To discuss the phase diagrams and Chern numbers of colored fermions with three internal states Red (R), Green (G) and Blue (B), we consider these fermions to be trapped in a two-dimensional square optical lattice. The Hamiltonian matrix or ultra-cold atoms with three

internal states is

$$\hat{\mathbf{H}} = \begin{pmatrix} \varepsilon_R(\hat{\mathbf{k}}) & -h_x/\sqrt{2} & 0 \\ -h_x/\sqrt{2} & \varepsilon_G(\hat{\mathbf{k}}) & -h_x/\sqrt{2} \\ 0 & -h_x/\sqrt{2} & \varepsilon_B(\hat{\mathbf{k}}) \end{pmatrix}, \quad (1)$$

when written in first quantization. In Eq. (1), the term

$$\varepsilon_R(\hat{\mathbf{k}}) = -2t\{\cos[(\hat{k}_x - k_T)a] + \cos[(\hat{k}_y - \mathcal{A}_y)a]\} \quad (2)$$

corresponds to the kinetic energy of the R state including the momentum transfer $+k_T$ along the x direction, arising from counter propagating Raman beams [26] or radio-frequency chips [38, 39], and the vector potential \mathcal{A}_y along the y direction, arising from laser assisted tunneling [15, 16]. The term

$$\varepsilon_G(\hat{\mathbf{k}}) = -2t\{\cos(\hat{k}_x) + \cos[(\hat{k}_y - \mathcal{A}_y)a]\} \quad (3)$$

corresponds to the kinetic energy of the G state, which experiences no momentum transfer, but feels the presence of \mathcal{A}_y , and

$$\varepsilon_B(\hat{\mathbf{k}}) = -2t\{\cos[(\hat{k}_x + k_T)a] + \cos[(\hat{k}_y - \mathcal{A}_y)a]\} \quad (4)$$

corresponds to the kinetic energy of B state, including the momentum transfer $-k_T$ along the x direction, and the vector potential \mathcal{A}_y along the y direction.

In Eqs. (2), (3), and (4), the parameter t is the hopping amplitude, a is the lattice spacing, k_T is the color-dependent momentum transfer along the x direction (artificial unidirectional color-orbit coupling), and $\mathcal{A}_y = eHx/\hbar c$ plays the role of the y -component of the artificial vector potential, where H is identified as a synthetic magnetic field along the z -axis. Notice that \mathcal{A}_y has dimensions of inverse length. It is important to emphasize that the system is neutral, so there is no charge e , that is, $\mathcal{A}_y a$ should be just viewed as a position dependent phase $\phi(x) = \mathcal{A}_y a$. Lastly, h_x represents a color-flip field along the x -direction, whose physical origin is a Rabi term that couples the Red and Green, as well as the Green and Blue internal states of the atom. As described in Sec. I, the vector potential \mathcal{A}_y may be generated by laser assisted tunneling [15, 16], while the color-dependent momentum transfer k_T and color-flip field h_x may be created via counter-propagating Raman beams [26] or via radio-frequency chips [38, 39].

The Hamiltonian matrix in Eq. (1) acts on a three-color wavefunction $\Psi(\mathbf{r}) = [\Psi_R(\mathbf{r}), \Psi_G(\mathbf{r}), \Psi_B(\mathbf{r})]^T$, where T indicates transposition and $\mathbf{r} = (x, y)$ labels the coordinates in the square lattice. An analogy to pseudo-spin-1 fermions or spin-1 bosons in optical lattices can be made by rewriting Eq. (1) in terms of spin-1 matrices \mathbf{J}_ℓ , with $\ell = \{x, y, z\}$ as

$$\hat{\mathbf{H}} = \varepsilon_G(\hat{\mathbf{k}})\mathbf{1} - h_x\mathbf{J}_x - h_z(\hat{\mathbf{k}})\mathbf{J}_z + g_z(\hat{\mathbf{k}})\mathbf{J}_z^2 \quad (5)$$

where h_x plays the role of a Zeeman field along the x axis in spin-space, $h_z(\hat{\mathbf{k}}) = [\varepsilon_B(\hat{\mathbf{k}}) - \varepsilon_R(\hat{\mathbf{k}})]/2$ represents momentum dependent Zeeman field along the z axis

in spin-space, and $g_z = [\varepsilon_B(\hat{\mathbf{k}}) + \varepsilon_R(\hat{\mathbf{k}})]/2 - \varepsilon_G(\hat{\mathbf{k}})$ describes a momentum dependent quadratic Zeeman shift along the z axis in spin-space, and thus can be viewed as a spin (color) quadrupolar effect. The color states $\{R, G, B\}$ are directly mapped into pseudo-spin-1 states $\{\uparrow, 0, \downarrow\}$. Notice that the presence of the color fields h_x , $h_z(\hat{\mathbf{k}})$ and $g_z(\hat{\mathbf{k}})$ breaks the $SU(3)$ symmetry of otherwise degenerate color bands. To make some connections to quantum chromodynamics (QCD), we note that the independent-particle Hamiltonian described in Eqs. (1) or (5) in general does not commute with the Gell-Mann matrices λ_j , which are the eight generators of $SU(3)$. To visualize this clearly, it is sufficient to recall that the angular momentum matrices \mathbf{J}_ℓ can be written in terms of λ_j as $\mathbf{J}_x = (\lambda_1 + \lambda_6)/2$; $\mathbf{J}_y = (\lambda_2 + \lambda_7)/2$; and $\mathbf{J}_z = (\lambda_3 + \sqrt{3}\lambda_8)/2$ and to show that the commutator $[\hat{\mathbf{H}}, \lambda_j] \neq 0$. The Hamiltonian in Eqs. (1) or (5) becomes $SU(3)$ invariant only when the fields $h_x = h_z(\hat{\mathbf{k}}) = g_z(\hat{\mathbf{k}}) = 0$, rendering $\hat{\mathbf{H}}$ diagonal and proportional to the unit matrix $\mathbf{1}$, that is, all color states become degenerate.

Having described the Hamiltonian of our system in this section, we discuss next the eigenspectrum associated with the Hamiltonian matrix described in Eqs. (1) or (5).

III. HARPER'S EIGENSPECTRUM

To obtain the eigenspectrum, it is important to establish the boundary conditions. We work in a cylindrical geometry having finite number N of sites along the x -direction but periodic boundary conditions along the y -direction. In the present case, k_y is a good quantum number, while k_x is not, and color-dependent Harper's matrix

$$\mathbf{H} = \begin{pmatrix} \mathbf{A}_{m-2} & \mathbf{B} & \mathbf{0} & \mathbf{0} & \mathbf{0} \\ \mathbf{B}^* & \mathbf{A}_{m-1} & \mathbf{B} & \mathbf{0} & \mathbf{0} \\ \mathbf{0} & \mathbf{B}^* & \mathbf{A}_m & \mathbf{B} & \mathbf{0} \\ \mathbf{0} & \mathbf{0} & \mathbf{B}^* & \mathbf{A}_{m+1} & \mathbf{B} \\ \mathbf{0} & \mathbf{0} & \mathbf{0} & \mathbf{B}^* & \mathbf{A}_{m+2} \end{pmatrix} \quad (6)$$

has a tridiagonal block structure that couples neighboring sites $(m-1, m, m+1)$ along the x -direction, but possesses discrete translational invariance along the y -axis. This is a generalization of the Harper's matrix for spin-1/2 fermions with two internal states [19]. The matrices \mathbf{A} , \mathbf{B} and the null matrix $\mathbf{0}$ consist of 3×3 blocks with entries labeled by internal color states $\{R, G, B\}$ or pseudo-spin-1 states $\{\uparrow, 0, \downarrow\}$. The size of the space labeled by the site index m is N , thus the total dimension of the matrix \mathbf{H} in Eq. (6) is $3N \times 3N$. The matrix indexed by position $x = ma$ is

$$\mathbf{A}_m = \begin{pmatrix} \mathbf{A}_{mR} & -h_x/\sqrt{2} & 0 \\ -h_x/\sqrt{2} & \mathbf{A}_{mG} & -h_x/\sqrt{2} \\ 0 & -h_x/\sqrt{2} & \mathbf{A}_{mB} \end{pmatrix},$$

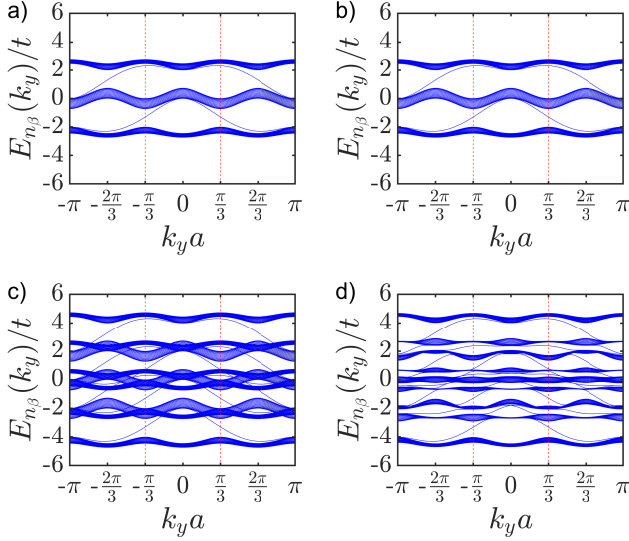


FIG. 1. (Color Online) Eigenvalues $E_{n_\beta}(k_y)/t$ of the color-dependent Harper's matrix versus $k_y a$ for magnetic flux ratio $\alpha = 1/3$. The parameters are: a) $k_T a = 0$ and $h_x/t = 0$, b) $k_T a = \pi/8$ and $h_x/t = 0$, c) $k_T a = 0$ and $h_x/t = 2$, d) $k_T a = \pi/8$ and $h_x/t = 2$. The vertical dashed lines located at $k_y a = \pm\pi/3$ indicate the boundaries of the magnetic Brillouin zone. The bulk bands have periodicity $2\pi/3a$, and the midgap edge bands have periodicity $2\pi/a$ along the k_y direction.

with $\mathbf{A}_{mR} = \mathbf{A}_{mG} = \mathbf{A}_{mB} = -2t \cos(k_y a - 2\pi m \alpha)$, where the parameter $\alpha = \Phi/\Phi_0$ represents the ratio between the magnetic flux through a lattice plaquette $\Phi = H a^2$ and the flux quantum $\Phi_0 = hc/e$, or the ratio between the plaquette area a^2 and the square of the magnetic length $\ell_M = \sqrt{hc/eH}$, that is, $\alpha = (a/\ell_M)^2$. The matrix that contains the color-orbit coupling is

$$\mathbf{B} = \begin{pmatrix} -te^{-ik_T a} & 0 & 0 \\ 0 & -t & 0 \\ 0 & 0 & -te^{ik_T a} \end{pmatrix},$$

where k_T ($-k_T$) corresponds to the momentum transfer along the x direction for state R (B), while the momentum transfer for state G is zero.

The full Hofstadter spectrum [20] of energy E versus flux ratio $\alpha = \Phi/\Phi_0$ for colored fermions can be obtained from the eigenvalues of the Harper's matrix defined in Eq. (6). However, in this work, we focus on a fixed value of α and discuss the energy spectrum as a function of the color-orbit coupling k_T and color-flip field h_x . We consider $N = 50$ sites along the x direction, with three states $\{R, G, B\}$ per site, but periodic boundary conditions along the y direction. The eigenvalues $E_{n_\beta}(k_y)$ are labeled by a discrete band index n_β and by momentum k_y , and are functions of the color-orbit coupling k_T , color-flip field h_x and flux ratio $\alpha = \Phi/\Phi_0$. The index β in n_β is a reminder that the resulting bands carry a mixed-color index β , when color is conserved, the index β labels $\{R, G, B\}$ states.

In Fig. 1, we show $E_{n_\beta}(k_y)$ for flux ratio $\alpha = 1/3$

in the cases: a) $k_T a = 0$ and $h_x/t = 0$, where there are three sets of degenerate bulk bands connected by color-degenerate midgap edge bands; b) $k_T a = \pi/8$ and $h_x/t = 0$, which is identical to case a) because of a color-gauge symmetry that allows gauging away the color-orbit coupling; c) $k_T a = 0$ and $h_x/t = 2$, where there are nine sets of bulk bands with regions of overlap (because color-degeneracies are only partially lifted by the color-flip field), and where there are color-dependent midgap edge bands connecting bulk bands; d) $k_T a = \pi/8$ and $h_x/t = 2$, where there are nine sets of bulk bands connected by color-dependent midgap edge states, but residual bulk band overlaps are lifted by the additional presence of color-orbit coupling. All bulk bands have momentum space periodicity of $2\pi/3a$, while all edge bands have period $2\pi/a$ along the k_y direction. It is important to point out that there are potential experimental techniques to image directly edge states [42] in the context of ultracold atoms. The periodicity of the bulk states is determined by the denominator q of the rational magnetic flux ratio $\alpha = p/q$, which for $\alpha = 1/3$ corresponds to $q = 3$. In Fig. 1, the vertical dashed lines specify the boundaries of the magnetic Brillouin zone at $k_y a = \pm\pi/3$.

Now that we have obtained the eigenspectrum of the system and identified the existence of midgap edge states connecting different mixed-color bands, we discuss next the associated Chern numbers for the colored fermions.

IV. COLOR CHERN NUMBERS

To identify topologically non-trivial mixed-color bands and extract their Chern indices, we impose periodic boundary conditions along the x and y directions, and compactify our cylinder into a torus. For rational $\alpha = p/q$, we write the color-dependent Harper's Hamiltonian as a $3q \times 3q$ matrix

$$\mathbf{H}(k_x, k_y) = \begin{pmatrix} \mathbf{H}_{RR} & \mathbf{H}_{RG} & \mathbf{H}_{RB} \\ \mathbf{H}_{GR} & \mathbf{H}_{GG} & \mathbf{H}_{GB} \\ \mathbf{H}_{BR} & \mathbf{H}_{BG} & \mathbf{H}_{BB} \end{pmatrix} \quad (7)$$

in momentum (k_x, k_y) space, by taking advantage of the magnetic translation group. We define $q \times q$ block matrices $\mathbf{H}_{cc'}$, where c and c' label the three color states $\{R, G, B\}$. The color-diagonal $q \times q$ block matrices \mathbf{H}_{cc} are

$$\begin{pmatrix} \Gamma_1 & -te^{ik_{xc}a} & 0 & \dots & -te^{-ik_{xc}a} \\ -te^{-ik_{xc}a} & \Gamma_2 & -te^{ik_{xc}a} & \dots & 0 \\ \vdots & \vdots & \vdots & \ddots & \vdots \\ -te^{ik_{xc}a} & 0 & \dots & -te^{-ik_{xc}a} & \Gamma_q \end{pmatrix},$$

where $k_{xc} = k_x - \gamma_c k_T$ is the color-dependent momentum along the x direction, including the color-dependent momentum transfer $\gamma_c k_T$, with $\gamma_R = +1$, $\gamma_G = 0$, and $\gamma_B = -1$. The kinetic energy terms are $\Gamma_m = -2t \cos(k_y a - 2\pi \alpha m)$, where the magnetic flux ratio is

$\alpha = p/q$ and m takes values $(1, \dots, q)$. The color-off-diagonal $q \times q$ block matrices are $\mathbf{H}_{RB} = \mathbf{H}_{BR} = \mathbf{0}$, and $\mathbf{H}_{RG} = \mathbf{H}_{GR} = \mathbf{H}_{GB} = \mathbf{H}_{BG} = \mathbf{H}_{\text{flip}}$, where

$$\mathbf{H}_{\text{flip}} = \begin{pmatrix} -h_x/\sqrt{2} & 0 & 0 & 0 & 0 \\ 0 & -h_x/\sqrt{2} & 0 & 0 & 0 \\ \vdots & \vdots & \vdots & \ddots & \vdots \\ 0 & 0 & \dots & 0 & -h_x/\sqrt{2} \end{pmatrix}, \quad (8)$$

describes color flips between R and G states, as well as, between G and B states, via the color-flip field h_x .

Next, we analyze the Chern numbers for different values of color-orbit coupling and color-flip fields, but fixed flux ratio $\alpha = p/q$. The energy spectrum associated with the Hamiltonian $\mathbf{H}(k_x, k_y)$ in Eq. (7) has $3q$ color-magnetic bands $E_{\ell_\gamma}(\mathbf{k})$ that are labeled by a magnetic band number ℓ_γ with generalized color index γ corresponding to mixed color states, which we identify as Cyan (C), Magenta (M) and Yellow (Y) or via a pseudo-spin basis $\{C, M, Y\} \rightarrow \{\uparrow, 0, \downarrow\}$. The minimum number of gaps between bulk bands is $q - 1$, when the bands are triply degenerate and the maximum is $3q - 1$, when there is no overlap between the bands.

The Chern index for the ℓ_γ^{th} band with generalized color index γ is

$$C_{\ell_\gamma} = \frac{1}{2\pi i} \int_{\partial\Omega} d^2\mathbf{k} F_{xy}^{(\ell_\gamma)}(\mathbf{k}), \quad (9)$$

where the domain of integration $\partial\Omega$ in momentum space corresponds to the magnetic Brillouin zone, that is, $\partial\Omega_x = [-\pi/a, \pi/a]$ along the k_x direction, and $\partial\Omega_y = [-\pi/qa, \pi/qa]$ along the k_y direction. The function

$$F_{xy}^{(\ell_\gamma)}(\mathbf{k}) = \partial_x A_y^{(\ell_\gamma)}(\mathbf{k}) - \partial_y A_x^{(\ell_\gamma)}(\mathbf{k}), \quad (10)$$

is the Berry curvature expressed in terms of the Berry connection $A_j^{(\ell_\gamma)}(\mathbf{k}) = \langle u_{\ell_\gamma}(\mathbf{k}) | \partial_j | u_{\ell_\gamma}(\mathbf{k}) \rangle$ where $|u_{\ell_\gamma}(\mathbf{k})\rangle$ are the eigenstates of the Hamiltonian $\mathbf{H}(k_x, k_y)$ defined in Eq. (7). In the limit of zero color-orbit coupling ($k_T = 0$) and zero color-flip field ($h_x = 0$), the energy spectrum for flux ratio $\alpha = p/q$ has triply-degenerate q magnetic bands and $q - 1$ gaps, such that the Chern index from Eq. (9) acquires a similar form to that found in the quantum Hall effect literature for spin-1/2 systems [43, 44].

Chern indices are properties of bands $E_{\ell_\gamma}(\mathbf{k})$ or band bundles with degeneracy D , and are computed using a discretized version of Eq. (9) via a generalization of the method used for spin-1/2 systems [45]. However, Chern numbers are defined within band gaps and depend on which gap the chemical potential is located. If the chemical potential μ is located in a band gap labelled by index r and corresponding to filling factor $\nu = r/q$, then the Chern number at this value of μ is

$$C_r = \sum_{\ell_\gamma, E < \mu}^{\nu=r/q} C_{\ell_\gamma}, \quad (11)$$

that is, the sum of Chern indices of bands with energies $E < \mu$, which characterize the insulating state labelled by the gap index r and filling factor $\nu = r/q$. Using our normalization, the maximum filling factor is $\nu_{\text{max}} = 3$. Furthermore, via the bulk-edge correspondence [46], the Chern number C_r calculated from the toroidal geometry (bulk system without edges) measures the total chirality of midgap edge states that are present in the cylindrical geometry. As described next, we use the Chern numbers defined in Eq. (11) to classify emergent topological phases in the phase diagrams of chemical potential μ versus color-flip field h_x and chemical potential μ versus color-orbit coupling k_T .

V. PHASE DIAGRAMS OF COLOR FERMIONS

Since we are interested in the effects of color-orbit coupling k_T and color-flip field h_x , we focus on phase diagrams for constant flux ratio $\alpha = p/q$, and choose the particular value of $\alpha = 1/3$, where non-trivial topological properties emerge. We use the Chern numbers defined in Eq. (11) to classify the topological phases in the phase diagrams of chemical potential μ versus color-flip field h_x and μ versus color-orbit coupling k_T . In some situations, a refinement is necessary to distinguish phases with the same *charge* Chern numbers, and we need to monitor the properties of the midgap edge states to expand the topological classification.

A. Chemical potential versus color-flip field

In Fig. 2, we show phase diagrams of chemical potential μ versus the color-flip field h_x for fixed value of the magnetic flux ratio $\alpha = 1/3$ with four values of the color-orbit parameter: a) $k_T a = 0$, b) $k_T a = \pi/8$, c) $k_T a = \pi/2$, and d) $k_T a = \pi$. From the figures, it is clear that phase diagrams are quite complex, in particular for values of $h_x/t > 1$. But, before we embark on the description of the phase diagrams for each figure, we discuss first the labelling of the regions indicated in the legend of the figure.

In Fig. 2, the white regions correspond to gapless (*conducting*) phases, where the chemical potential lies within a band of states, while the non-white (colored) regions correspond to insulating phases, where the chemical potential lies within the gaps between bands of states. The legend in this figure is a color palette describing the Chern numbers for each colored region: +3 (magenta), +2 (blue), +1 (red, red-with-black-dots and dark red), 0 (gray, black, orange), -1 (yellow, yellow with black dots and dark yellow), -2 (green), -3 (cyan). There are also very small regions with Chern numbers ± 6 only seen in Fig. 2b. Given that certain regions with different colors have the same Chern numbers, it is clear that additional properties are needed to distinguish them. Before we discuss the phase diagrams in more detail, we describe

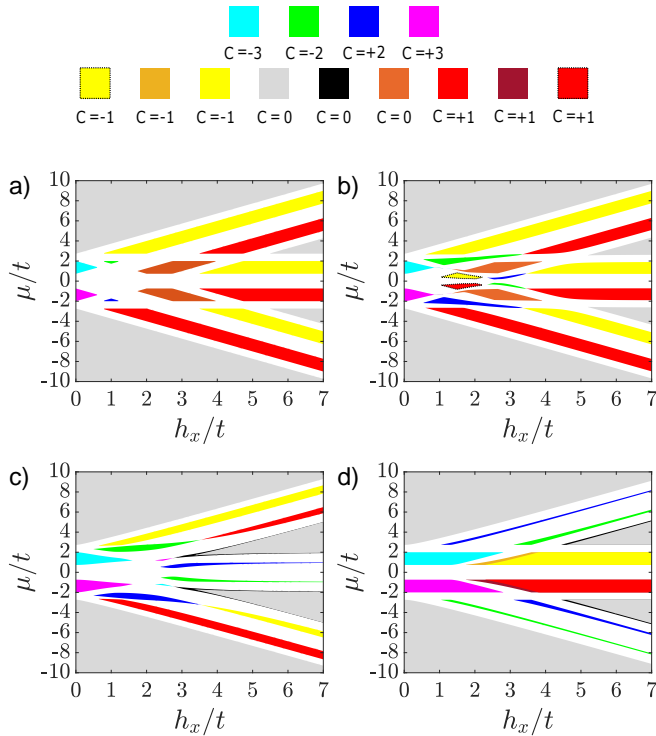


FIG. 2. (Color Online) Phase diagrams of chemical potential μ/t versus Zeeman field h_x/t and the associated Chern numbers are shown for spin-orbit coupling parameters: a) $k_{Ta} = 0$, b) $k_{Ta} = \pi/8$, c) $k_{Ta} = \pi/2$, and d) $k_{Ta} = \pi$. The white regions correspond to gapless (conducting) phases, where the chemical potential lies within a band of states, while the non-white regions correspond to insulating phases, where the chemical potential lies within the gaps between bands of states. As shown in the color palette (legend), the Chern numbers for each colored region are +3 (magenta), +2 (blue), +1 (red, red-with-black-dots and dark red), 0 (gray, black, orange), -1 (yellow, yellow-with-black-dots and dark yellow), -2 (green), and -3 (cyan).

first the color palette. The magenta (cyan) regions with Chern number +3 (-3) possess three chiral midgap edge states with positive (negative) chirality, while the blue (green) regions with Chern number +2 (-2) possess two chiral midgap edge states with positive (negative) chirality. The red (yellow) regions with Chern number +1 (-1) possess one chiral midgap edge state with positive (negative) chirality; the dark red (dark yellow) regions with Chern number +1 (-1) possess not only one chiral midgap edge state with positive (negative) chirality, but also present achiral midgap edge states, nevertheless they are not topologically distinct from their parent red (yellow) regions. However, the red-with-black-dots (yellow-with-black-dots) regions with Chern number +1 (-1) have three chiral midgap edge states, two of which have positive (negative) chirality, and one of which has negative (positive) chirality. Therefore, these insulating regions are topologically distinct from the red (yellow) regions with the same Chern numbers. The gray regions

with Chern number 0 are topologically trivial with no chiral or achiral midgap edge states. The black regions with Chern number 0 are also topologically trivial with no chiral midgap edge states but with achiral midgap edge states. These black regions are not topologically distinct from the gray regions. Lastly, the orange regions with Chern number 0 are topologically non-trivial and possess two chiral midgap edge states with opposite chirality, reminiscent of the quantum spin-Hall effect in spin-1/2 fermions.

Before we analyze the details of the phase diagrams shown in Figs. 2a through 2d, we discuss first some of their general properties. The first thing to notice is that the phase diagrams are particle-hole symmetric with respect to the line $\mu = 0$, this means that the Chern numbers have odd symmetry upon reflection through $\mu = 0$, since they represent the total chirality of edge states. A change in the *charge* from particle-like to hole-like leads to a flip in the chirality of the edge states, that is, a change in sign of the Chern number defined in Eq. (11). The particle-hole symmetry in the Chern number spectrum reflects the same symmetry present in the Hamiltonian for this problem.

For fixed flux ratio $\alpha = 1/3$ and color-orbit parameter k_{Ta} , the number of insulating phases, where gaps between energy bands exist, grows from two to eight with increasing color-flip parameter h_x/t from $h_x/t \ll 1$ to $h_x/t \gg 1$. This situation does not occur in electronic systems with spin-1/2 since the Zeeman field h_x cannot be tuned independently from the magnetic ratio α as they have the same origin, and typically h_x has very small values in comparison to the hopping parameter t , such that $h_x/t \ll 1$. However, for ultracold fermions, since h_x is a synthetic field that can be tuned independently from the magnetic ratio α , it can attain high values in comparison to t and provide access to phases that are not encountered in standard condensed matter systems.

In the regime $h_x/t \ll 1$, where the color splitting caused by the color-flip field h_x is small in comparison to the hopping t , the energy spectrum has only two gaps similar to the cases illustrated in Figs. 1a and 1b. Thus, only two insulating phases emerge: one with Chern number +3 (magenta region) at the first gap and the other -3 (cyan region) at the second gap. These phases are the color generalizations of the quantum Hall phases for spin-1/2 systems, which have Chern numbers +2 and -2. In the phase with Chern number +3, there are three chiral midgap edge states with positive chirality, and in the phase with Chern number -3 there are three chiral midgap edge states with negative chirality. Hence, these are essentially color unpolarized phases.

In the regime $h_x/t \gg 1$, where the color splitting caused by the color-flip field h_x is large in comparison to the hopping t , in which case the system is essentially polarized in a mixed-color basis of the color (pseudo-spin) matrix \mathbf{J}_x described in Eq. (5). In this case, the color-orbit parameter k_{Ta} lifts band degeneracies and creates eight gapped phases. In Figs. 2a and 2b where $k_{Ta} \ll \pi$,

the eight color-insulating phases have Chern numbers $+1$ (red regions), -1 (yellow regions), and 0 (gray regions), when $h_x/t \gg 1$. However, when color-orbit coupling $k_T a$ is sufficiently large, the mixed color-bands get strongly coupled and the nature of the insulating phases changes dramatically. For $k_T a = \pi/2$, the insulating states have Chern numbers $+1$ (red regions), -1 (yellow regions), 0 (gray regions), -2 (green region) and $+2$ (blue region); while for $k_T a = \pi$, the insulating phases have -2 (green regions), $+2$ (blue regions), 0 (gray regions), $+1$ (red region), and -1 (yellow region).

In Fig. 2a, where $k_T a = 0$, we can see many different insulating phases in the chemical potential versus color-flip field diagram as h_x/t is changed. Each of these insulating phases corresponds to a fixed filling factor $\nu = r/3$, where r is an integer that represents a gap, varying from 0 to 9 . Zero filling factor $\nu = 0$ corresponds to $r = 0$, and full filling factor $\nu = 3$ corresponds to $r = 9$, these correspond to the lower and upper gray regions respectively, which are topologically trivial with zero Chern number. Viewing the μ/t versus h_x/t phase diagram through the lens of filling factors ν reveals that there is one insulating phase with filling factor $\nu = 1/3$ (lower red region), two insulating phases with $\nu = 2/3$ (blue and lower yellow regions), three insulating phases with $\nu = 1$ (magenta, lower orange and lower gray regions), one insulating phase with $\nu = 4/3$ (middle red region), one insulating phase with $\nu = 5/3$ (middle yellow region), three insulating phases with $\nu = 2$ (cyan, upper orange and upper gray regions), two insulating phases with $\nu = 7/3$ (green and upper red regions), and one insulating phase with $\nu = 8/3$ (upper yellow region).

The most interesting feature in Fig. 2a are the orange regions around $\mu = 0$ with filling factors $\nu = 1$ and 2 , which possess zero Chern number, but have two chiral midgap edge states with opposite chiralities, producing a phase that we name quantum color Hall (QCoH) insulator, in analogy to the quantum spin Hall (QSH) insulator that exhibits the quantum spin-Hall effect. These orange regions are the color versions of the QSH phases for spin-1/2 fermions [27–29].

The phase diagram in Fig. 2b, where $\alpha = 1/3$ and $k_T a = \pi/8$, has the most unconventional phases and phase transitions. The insulating phases for fixed filling factor are as follows. At filling factors $\nu = 0$ and $\nu = 3$, the bands are either completely empty or completely full, leading to the topological trivial insulating gray regions. At filling factor $\nu = 1/3$, there is one insulating phase (lower red region). At filling factor $\nu = 2/3$, there are two insulating phases (blue and yellow regions) and a direct topological quantum phase transition between blue and yellow regions at $h_x/t = 3.35$, and by particle-hole symmetry, there are also, at filling factor $\nu = 7/3$, two insulating phases (green and red regions) and a direct topological phase transition between the green and red regions at the same color-flip field $h_x/t = 3.35$. At filling factor $\nu = 1$, there are five insulating phases. Starting from the magenta region, as h_x/t grows, there is a direct topolog-

ical quantum phase transition at $h_x/t = 0.85$ to a very thin and small dark magenta region with Chern number $+6$, which exists between $0.85 < h_x/t < 1.10$, and leads to a *conducting* phase between $1.10 < h_x/t < 1.20$. Then another very thin and small magenta region emerges between $1.20 < h_x/t < 1.35$, leading to an additional direct topological quantum phase transition into the orange region at $h_x/t = 1.35$. Finally, at high values of h_x/t , a topologically trivial gray region emerges.

By particle-hole symmetry, at filling factor $\nu = 2$ there are also five insulating phases, which have Chern numbers opposite to the ones for $\nu = 1$. Starting from the cyan region, as h_x/t grows, there is direct topological quantum phase transition at $h_x/t = 0.85$ to a very thin and small dark cyan region with Chern number -6 , which exists between $0.85 < h_x/t < 1.10$, and leads to a *conducting* phase between $1.10 < h_x/t < 1.20$. Then another very thin and small cyan region emerges between $1.2 < h_x/t < 1.35$, leading to an additional direct topological quantum phase transition into the orange region at $h_x/t = 1.35$. Finally, at high values of h_x/t , a topologically trivial gray region emerges.

At filling factor $\nu = 4/3$, there are three insulating phases as h_x/t grows (red-with-black-dots, green and red regions). There is a direct topological quantum phase transition between the green and red regions at $h_x/t = 3.45$. The green region with two chiral midgap edge states with negative chirality and the red region with one chiral midgap edge state with positive chirality exhibit the standard quantum Hall effect, which we name from now on as the quantum charge Hall (QChH) effect. The red-with-black-dots region contains three midgap edge states, two with positive chirality and one with negative chirality, thus possessing the QChH effect, however, two of the midgap edge states with opposite chirality, have also different mixed-color indices leading to a quantum color Hall (QCoH) effect. This situation is analogous to the quantum spin Hall effect for spin-1/2 fermions.

Again, by particle-hole symmetry, at filling factor $\nu = 5/3$, there are three insulating phases with growing h_x/t (yellow-with-black-dots, blue and yellow regions). There is a direct topological quantum phase transition between the green and red regions at $h_x/t = 3.45$. The blue region with two chiral midgap edge states with positive chirality and the yellow region with one chiral midgap edge state with negative chirality exhibit the standard QChH effect. The yellow-with-black-dots region contains three midgap edge states, two with negative chirality and one with positive chirality, leading to net negative chirality and the QChH effect. Furthermore, since midgap edge states with opposite chirality have different mixed-color indices, this phase also exhibits a QCoH effect.

In Fig. 2c, with $\alpha = 1/3$ and $k_T a = \pi/2$, the insulating phases for fixed filling factor ν are as follows. At filling factors $\nu = 0$ and $\nu = 3$, the bands are either completely empty or completely full, leading to the topological trivial insulating gray regions. For $\nu = 1/3$, there

is only the lower red region, and by particle-hole symmetry, for $\nu = 8/3$, there is only the upper yellow region. For $\nu = 2/3$, there are two insulating phases (blue and yellow regions) with a direct topological quantum phase transition between the two of them at $h_x/t = 3.55$, and again by particle-hole symmetry, for $\nu = 7/3$, there are two insulating phases (green and red regions) with a direct topological quantum phase transition between them at $h_x/t = 3.55$. For $\nu = 1$, there are four insulating phases (magenta, cyan, black and gray regions) with a direct topological quantum phase transition between the cyan and black phases at $h_x/t = 2.75$. A crossover line between the black and gray regions occurs where achiral midgap edge states from the black regions merge into the bulk of the gray regions, which possess no midgap edge states. Again, by particle-hole symmetry, at $\nu = 2$ there are four insulating phases (cyan, magenta, black and gray regions) with a direct topological quantum phase transition between the magenta and black phases at $h_x/t = 2.75$. A crossover line between the black and gray regions occurs where the achiral midgap edge states from the black regions merge into the bulk of the gray regions, which possess no midgap edge states.

In Fig. 2d, with $\alpha = 1/3$ and $k_T a = \pi$, the insulating phases for fixed filling factor are as follows. At filling factors $\nu = 0$ and $\nu = 3$, the bands are either completely empty or completely full, leading to the topological trivial insulating gray regions. For filling factor $\nu = 1/3$, there is one insulating phase (lower green region). For $\nu = 2/3$, there is one insulating phase (lower blue region). For $\nu = 1$, there are three insulating phases (magenta, black and gray regions): the black and gray regions are separated by a line, where achiral midgap edge states from the black region merge into the bulk leading to the gray regions with no midgap edge states. For $\nu = 4/3$, there are two insulating phases (dark red and red regions) separated by a crossover line, where achiral midgap edge states from the dark red region merge into the bulk leading to the red region with a single chiral midgap edge state with positive chirality.

The rest of the phase diagram can be obtained by particle-hole symmetry. For $\nu = 5/3$, there are two insulating phases (dark yellow and yellow regions) separated by a crossover line, where achiral edge states, that exist in the dark yellow region, merge into the bulk leading to the yellow region with one chiral midgap edge state with negative chirality. For $\nu = 2$, there are three insulating phases (cyan, black and gray regions). The black and gray regions are separated by a line where achiral midgap edge states from the black region merge into the bulk leading to the gray regions with no midgap edge states. For $\nu = 7/3$, there is one insulating phase (upper green region). For $\nu = 8/3$, there is one insulating phase (upper blue region). We highlight that the dark red and dark yellow regions have not only one topologically non-trivial chiral midgap edge band, but also topologically trivial achiral midgap edge states. However the dark red and dark yellow regions are not topologically

distinct from the red and yellow regions which have only one topologically non-trivial chiral midgap edge band.

In the analysis of different panels of the chemical potential μ/t versus color-flip fields h_x/t shown in Fig. 2, we have seen that the filling factor $\nu = r/q$ can be used as a label for the insulating phases, because when the chemical potential μ varies within a gap, the filling factor remains constant, as the insulating state is incompressible. Thus, next, we generalize the gap-labelling theorem found for spin-1/2 fermions for fixed magnetic flux parameter α , and extend it to fermions with three internal states.

B. Gap Labelling Theorem

For spin-1/2 fermions in condensed matter systems, a gap labelling theorem that relates the filling factor $\nu = r/q$ and the magnetic flux parameter $\alpha = \Phi/\Phi_0 = p/q$ was found by Wannier and Claro [47, 48]. In that case, the Zeeman field h_x was neglected and the theorem covered only couplings to the charge degrees of freedom of the system. However, in the present case, it is clear that the color-flip fields h_x play an important role in creating additional gaps, as we have seen in the discussion of Fig. 2. As h_x/t varies from $h_x/t \ll 1$ to $h_x/t \gg 1$ the number of gaps grows from two (2) to eight (8). From the analysis of Fig. 2, it is clear that the filling factor ν associated with gap r is a good label for the insulating phases, as are the Chern numbers C_r .

We can establish a relation between the Chern numbers C_r , the magnetic ratio $\alpha = p/q$ and the filling factor $\nu = r/q$ by rewriting the Diophantine equation

$$r = qS_r + pC_r, \quad (12)$$

where the integer index r labels the gaps in the energy spectrum $E_{\ell_\gamma}(k_x, k_y)$ of the toroidal geometry, C_r is the Chern number for the r^{th} gap and S_r is a supplementary topological invariant. This equation can be rewritten in terms of the filling factor $\nu = r/q$ and the magnetic ratio $\alpha = p/q$ as

$$\nu = S_r + \alpha C_r. \quad (13)$$

The relation shown above generalizes the gap labelling theorem [47, 48] used in the context of the integer quantum-Hall effect, because the topological quantum numbers (S_r, C_r) change not only as a function of the magnetic ratio α , but also as a function of the color-flip field h_x/t and color-orbit parameter $k_T a$, that is, $S_r(h_x/t, k_T a)$ and $C_r(h_x/t, k_T a)$. Notice that the maximal value of S_r for a given gap labeled by r is linked to the minimum value of C_r and vice-versa, that is, $S_{r,\text{max}} = \nu - \alpha C_{r,\text{min}}$ and $S_{r,\text{min}} = \nu - \alpha C_{r,\text{max}}$.

For three color states, the integer values of r range from 0 (when $\nu = 0$) to $3q$ (when $\nu = 3$). In the phase diagrams of μ/t versus h_x/t or μ/t versus $k_T a$, the locations where the gaps open change as a function of h_x/t

and $k_T a$, but the gap labelling relation given in Eq. (13) applies to all insulating phases. Just to mention a couple of examples for $\alpha = 1/3$, the five insulating phases with filling factor $\nu = 1$ ($r = 3$) in Fig. 2b have topological labels (S_3, C_3) that vary as a function of the color-flip field h_x/t . The sequence of insulating phases from low to high h_x/t is magenta with $(0, +3)$, dark magenta $(-1, +6)$, magenta with $(0, +3)$, orange with $(+1, 0)$, and gray with $(+1, 0)$. While for the case of $\nu = 2$ ($r = 6$) in Fig. 2b the sequence of insulating phases with growing h_x/t is cyan with $(+3, -3)$, dark cyan with $(+4, -6)$, cyan with $(+3, -3)$, orange with $(+2, 0)$, and gray with $(+2, 0)$.

Having introduced the gap labelling relation that connects filling factors ν , magnetic flux ratio α and topological numbers (S_r, C_r) , we will use this ordered pair to classify the topological phases in the *charge* sector, noting that additional topological numbers may arise in the *color* sector, for instance in the phase diagram of μ/t versus $k_T a$ discussed next.

C. Chemical potential versus color-orbit coupling

In Fig. 3, we show phase diagrams of chemical potential μ/t versus spin-orbit parameter $k_T a$ for fixed magnetic ratio $\alpha = 1/3$ and changing color-flip fields: a) $h_x/t = 0$, b) $h_x/t = 1$, c) $h_x/t = 2$ and d) $h_x/t = 3$. The color palette for insulating phases is the same used in Fig. 2 with six additional very small regions with Chern numbers $+6$ (dark magenta) at $\nu = 1$ and -6 (dark cyan) at $\nu = 2$ in Fig. 3b; Chern numbers $+2$ (dark green) at $\nu = 4/3$ and -2 (light blue) at $\nu = 5/3$ in Fig. 3c; and Chern numbers $+5$ (light brown) at $\nu = 2/3$ and -5 (light-pink) at $\nu = 7/3$ in Fig. 3d. Before we go into the details of each panel of Fig. 3, we point out a few general properties. We notice that the phase diagram of μ/t versus $k_T a$ has periodicity of 2π , inversion symmetry with respect to $k_T a = \pi$, and particle-hole symmetry with respect to $\mu = 0$. All these properties arise directly from symmetries of the Hamiltonian of the system discussed in Sec. II. Furthermore, for fixed h_x/t , there are several topological quantum phase transitions that occur between different insulating phases as $k_T a$ is changed. Notice also that the lower and upper gray regions are topologically trivial and correspond to $\nu = 0$ with $(S_0, C_0) = (0, 0)$, and $\nu = 3$ with $(S_9, C_9) = (+3, 0)$, respectively.

In Fig. 3a, where $\alpha = 1/3$ and $h_x/t = 0$, the phase diagram of μ/t versus $k_T a$ has only two topological insulating phases. The first one is the magenta region at $\nu = 1$ with $(S_3, C_3) = (0, +3)$, and the second is the cyan region at $\nu = 2$, with $(S_6, C_6) = (+3, -3)$. These regions are independent of $k_T a$ because the color-orbit coupling k_T can be gauged away for $h_x/t = 0$, that is, the Hamiltonian exhibits a color-gauge symmetry. This leads to an energy spectrum that is independent of $k_T a$ (see for example Figs. 1a and 1b), and therefore the phase dia-

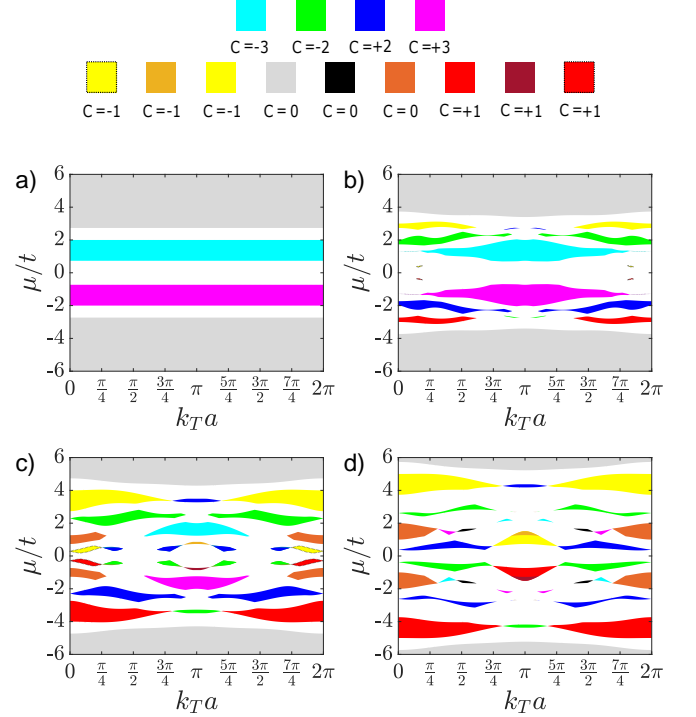


FIG. 3. (Color Online) Chemical potential μ/t versus spin-orbit parameter $k_T a$ for flux ratio $\alpha = 1/3$ and Zeeman fields: a) $h_x/t = 0$, b) $h_x/t = 1$, c) $h_x/t = 2$, d) $h_x/t = 3$. The color palette for insulating phases is the same used in Fig. 2 with six additional very small regions with Chern numbers $+6$ (dark magenta) at $\nu = 1$ and -6 (dark cyan) at $\nu = 2$ in Fig. 3b; Chern numbers $+2$ (dark green) at $\nu = 4/3$ and -2 (light blue) at $\nu = 5/3$ in Fig. 3c; and Chern numbers $+5$ (light brown) at $\nu = 2/3$ and -5 (light-pink) at $\nu = 7/3$ in Fig. 3d.

grams for all $k_T a$ are identical to the phase diagram for $k_T a = 0$. At $h_x/t = 0$, the color-gauge symmetry of the Hamiltonian leads to topological numbers S_r and C_r that are independent of the color-orbit coupling parameter $k_T a$.

In Fig. 3b, where $\alpha = 1/3$ and $h_x/t = 1$, there are many more topological insulating phases and additional filling factors. At $\nu = 1/3$, there are red regions with $(S_1, C_1) = (0, +1)$ and green regions with $(S_1, C_1) = (1, -2)$. At $\nu = 2/3$, there are blue regions with $(S_2, C_2) = (0, +2)$. At $\nu = 1$, there are very thin dark magenta regions $(S_3, C_3) = (-1, +6)$ close to $k_T a = 0.17\pi$ and $k_T a = 1.83\pi$ that have direct topological quantum phase transitions to the central magenta region with $(S_3, C_3) = (0, +3)$. At $\nu = 4/3$, there are small red-with-black-dots regions with $(S_4, C_4) = (+1, +1)$. At $\nu = 5/3$, there are small yellow-with-black-dots regions with $(S_5, C_5) = (+2, -1)$. At $\nu = 2$, there are very thin dark cyan regions $(S_6, C_6) = (+4, -6)$ close to $k_T a = 0.17\pi$ and $k_T a = 1.83\pi$ that have direct topological quantum phase transitions to the central cyan region with $(S_6, C_6) = (+3, -3)$. At $\nu = 7/3$, there are green regions with $(S_7, C_7) = (+3, -2)$. At $\nu = 8/3$, there are yellow regions with $(S_8, C_8) = (+3, -1)$ and blue regions

with $(S_8, C_8) = (+2, +2)$.

In Fig. 3c, where $\alpha = 1/3$ and $h_x/t = 2$, the phase diagram is even richer than in the case of Fig. 3b. At $\nu = 1/3$, there are red regions with $(S_1, C_1) = (0, +1)$ and green regions with $(S_1, C_1) = (1, -2)$, and direct topological quantum phase transitions between them at $k_T a = 0.81\pi$ and $k_T a = 1.19\pi$. At $\nu = 2/3$, there are blue regions with $(S_2, C_2) = (0, +2)$. At $\nu = 1$, there are orange regions with $(S_3, C_3) = (+1, 0)$ and magenta regions with $(S_3, C_3) = (0, +3)$. The orange regions are very special, because they have two chiral midgap edge states with opposite chirality, and although they do not produce a quantum charge Hall (QChH) effect, they possess a quantum color Hall (QCoH) effect, similar to the quantum spin Hall effect for spin-1/2 fermions. At $\nu = 4/3$, there are red-with-black-dots and dark red regions with $(S_4, C_4) = (+1, +1)$ and dark green and green regions with $(S_4, C_4) = (+2, -2)$. There are direct topological quantum phase transitions between the red-with-black-dots and dark green regions at $k_T a = 0.25\pi$ and $k_T a = 1.75\pi$. The red-with-black-dots regions have three chiral midgap edge states, two with positive and one with negative chirality, thus this phase possesses simultaneously quantum charge Hall (QChH) and quantum color Hall (QCoH) effects, a situation that has no correspondence for spin-1/2 fermions. The dark green regions have two chiral midgap edge states with negative chirality and achiral midgap edge states. When the achiral midgap edge states merge into the bulk, the dark green regions cross over to the green regions. There are also direct topological quantum phase transitions between the dark green and dark red regions at $k_T a = 0.90\pi$ and $k_T a = 1.10\pi$. The dark red region has one chiral midgap edge state with positive chirality, and at least one achiral midgap edge state.

The rest of the phases of Fig. 3c can be analyzed using particle-hole symmetry. At $\nu = 5/3$, there are yellow-with-black-dots and dark yellow regions with $(S_5, C_5) = (+2, -1)$ and light blue and blue regions with $(S_5, C_5) = (+1, +2)$. There are direct topological quantum phase transitions between the yellow-with-black-dots and light blue regions at $k_T a = 0.25\pi$ and $k_T a = 1.75\pi$. The yellow-with-black-dots regions have three chiral midgap edge states, two with negative and one with positive chirality, thus this phase possesses simultaneously quantum charge Hall (QChH) and quantum color Hall (QCoH) effects, a situation that has no correspondence for spin-1/2 fermions. The light blue regions have two chiral midgap edge states with positive chirality and achiral midgap edge states. When the achiral midgap edge states merge into the bulk, the light blue regions cross over to the blue regions. There are also direct topological quantum phase transitions between the light blue and dark yellow regions at $k_T a = 0.90\pi$ and $k_T a = 1.10\pi$. The dark yellow regions have one chiral midgap edge state with negative chirality, and at least one achiral midgap edge state. At $\nu = 2$, there are orange regions with $(S_6, C_6) = (+2, 0)$ and cyan regions with

$(S_6, C_6) = (+3, -3)$. Again, the orange regions are very special, because they have two chiral midgap edge states with opposite chirality, and although they do not produce a quantum charge Hall (QChH) effect, they possess a quantum color Hall (QCoH) effect, similar to the quantum spin Hall effect for spin-1/2 fermions. At $\nu = 7/3$, there are green regions with $(S_7, C_7) = (+3, -2)$. At $\nu = 8/3$, there are yellow regions with $(S_8, C_8) = (+3, -1)$ and blue regions with $(S_8, C_8) = (+2, +2)$, and direct topological quantum phase transitions between them at $k_T a = 0.81\pi$ and $k_T a = 1.19\pi$.

In Fig. 3d, where $\alpha = 1/3$ and $h_x/t = 3$, the phase diagram is as rich as in Fig. 3c. The main differences between the two figures are the emergence of very small light brown regions at $\nu = 2/3$ with $(S_2, C_2) = (-1, +5)$ near $k_T a = \pi$; the emergence of cyan regions with $(S_3, C_3) = (+2, -3)$ and black regions with $(S_3, C_3) = (+1, 0)$ at $\nu = 1$; the disappearance of the red-with-black-dot regions $(S_4, C_4) = (+1, +1)$ and the merger of green regions with $(S_4, C_4) = (+2, -2)$ at $\nu = 4/3$. Similar effects occur to the phases with $\mu > 0$ by particle-hole symmetry around $\mu = 0$, that is, for the mapping $\nu = r/3 \rightarrow 3 - \nu$ with $C_r \rightarrow -C_{9-r}$. At $\nu = 1/3$, there are red regions with $(S_1, C_1) = (0, +1)$ and green regions with $(S_1, C_1) = (+1, -2)$, and direct topological quantum phase transitions between them at $k_T a = 0.82\pi$ and $k_T a = 1.18\pi$. At $\nu = 2/3$, there are blue regions with $(S_2, C_2) = (0, +2)$ and very small light brown regions $(S_2, C_2) = (-1, +5)$ near $k_T a = \pi$ that have a direct topological quantum phase transition into also very small new blue regions at $k_T a = 0.90\pi$ and $k_T a = 1.10\pi$. At $\nu = 1$, there are orange regions with $(S_3, C_3) = (+1, 0)$, cyan regions with $(S_3, C_3) = (+2, -3)$ and black regions with $(S_3, C_3) = (+1, 0)$. There are also direct topological quantum phase transitions from the orange to the cyan regions at $k_T a = 0.31\pi$ and $k_T a = 1.69\pi$, as well as, from cyan to black regions at $k_T a = 0.46\pi$ and $k_T a = 1.54\pi$. At $\nu = 4/3$, there are green regions with $(S_4, C_4) = (+2, -2)$, as well as red and dark red regions with $(S_4, C_4) = (+1, +1)$. There are direct topological quantum phase transitions between the green and red regions at $k_T a = 0.74\pi$ and $k_T a = 1.24\pi$. Notice that the dark red region crosses over into the red region (around $k_T a = \pi$), when all its achiral midgap edge states merge into the bulk.

The additional phases of Fig. 3d reflect particle-hole symmetry about $\mu = 0$. At $\nu = 5/3$, there are blue regions with $(S_5, C_5) = (+1, +2)$ and yellow and dark yellow regions with $(S_5, C_5) = (+2, -1)$. There are direct topological quantum phase transitions between the blue and yellow regions at $k_T a = 0.74\pi$ and $k_T a = 1.26\pi$. Notice that the dark yellow region crosses over into the yellow region (around $k_T a = \pi$), when all its achiral midgap edge states merge into the bulk. At $\nu = 2$, there are orange regions with $(S_6, C_6) = (+2, 0)$, magenta regions with $(S_6, C_6) = (+1, +3)$ and black regions with $(S_6, C_6) = (+2, 0)$. There are also direct topological quantum phase transitions from the orange to the ma-

genta regions at $k_T a = 0.31\pi$ and $k_T a = 1.69\pi$, as well as, from the magenta to black regions at $k_T a = 0.46\pi$ and $k_T a = 1.54\pi$. At $\nu = 7/3$, there are green regions with $(S_7, C_7) = (+3, -2)$ and very small light pink regions $(S_7, C_7) = (+4, -5)$ near $k_T a = \pi$ that have direct topological quantum phase transitions into very small new green regions at $k_T a = 0.90\pi$ and $k_T a = 1.10\pi$. At $\nu = 8/3$, there are yellow regions with $(S_8, C_8) = (+3, -1)$ and blue regions with $(S_8, C_8) = (+2, +2)$, and direct topological quantum phase transitions between them at $k_T a = 0.82\pi$ and $k_T a = 1.18\pi$.

From the analysis of the phase diagrams in Figs. 3 and 4, we have established that there is a staircase of filling factor ν versus chemical potential μ labeled by topological quantum numbers (S_r, C_r) at every gap r in the energy spectrum. The steps of the staircase structure occur at values of ν given by the gap labelling theorem displayed in Eq. (13). To make this connection more evident, we analyze next the color density of states $\rho_c(E)$ and the total color density of states $\rho(E) = \sum_c \rho_c(E)$. From $\rho(E)$, we compute directly the filling factor ν as a function of chemical potential μ and show that there are steps in the function $\nu(\mu)$ at the precise values determined by the gap labelling theorem. This indicates the existence of incompressible insulating phases labeled by the topological indices (S_r, C_r) at $\nu = r/q$, as expected.

VI. COLOR DENSITY OF STATES

In conjunction with the energy spectrum $E_{n_\beta}(k_y)$ with open boundary conditions or $E(k_x, k_y)$ with periodic boundary conditions for fixed magnetic flux $\alpha = p/q$, the total color density of states $\rho(E)$ and the color density of states $\rho_c(E)$ for color c are useful quantities to identify the location of gapped phases as a function of color-flip fields h_x/t and color-orbit coupling $k_T a$.

The density of states can be obtained from the Green (Resolvent) operator

$$\hat{\mathbf{G}}(z) = \frac{1}{z\mathbf{1} - \hat{\mathbf{H}}}, \quad (14)$$

whose matrix elements in the original color basis $\{R, G, B\}$ can be written as

$$G_{cc'}(z) = \sum_{n_\beta k_y} \frac{u_{n_\beta c}(k_y) u_{n_\beta c'}^*(k_y)}{z - E_{n_\beta}(k_y)} \quad (15)$$

where $u_{n_\beta c}(k_y)$ are the color components of the eigenvectors of the Hamiltonian operator $\hat{\mathbf{H}}$ with open boundary conditions and eigenvalues $E_{n_\beta}(k_y)$. The summations over k_y cover the magnetic Brillouin zone $[-\pi/qa, \pi/qa]$ for bulk states and the range $[-\pi/a, \pi/a]$ for midgap edge states, where a is the square lattice unit cell length, and include all mixed-color band indices n_β . Using the appropriate spectral decomposition for the case with periodic

boundary conditions, we obtain

$$G_{cc'}(z) = \sum_{\ell_\gamma k_x k_y} \frac{u_{\ell_\gamma c}(k_x, k_y) u_{\ell_\gamma c'}^*(k_x, k_y)}{z - E_{\ell_\gamma}(k_x, k_y)}, \quad (16)$$

where $u_{\ell_\gamma c}(k_x, k_y)$ are the color components of the eigenvectors of the Hamiltonian operator $\hat{\mathbf{H}}$ with periodic boundary conditions and eigenvalues $E_{\ell_\gamma}(k_x, k_y)$. Here, ℓ_γ labels the magnetic subbands for $\alpha = p/q$. The momentum summations are over $[-\pi/a, \pi/a]$ for k_x and over $[-\pi/qa, \pi/qa]$ for k_y , that is, the summations over $\{\ell_\gamma, k_x, k_y\}$ cover the magnetic Brillouin zone and all the mixed color bands labelled by ℓ_γ .

Within the magnetic Brillouin zone, the density of states of color c at energy E is

$$\bar{\rho}_c(E) = -\frac{1}{\pi} \lim_{\delta \rightarrow 0} \text{Im} G_{cc}(z = E + i\delta), \quad (17)$$

where δ is a small imaginary part. The color density of states per site is

$$\rho_c(E) = \frac{\bar{\rho}_c(E)}{q}, \quad (18)$$

since there are q unit cells in real space. The color density of states $\bar{\rho}_c(E)$ in the magnetic unit cell integrates to q states over all energies. The color density of states per site $\rho_c(E)$ always integrates to 1, because we have a maximum of one state for a given color c . Within the magnetic Brillouin zone, the number of states of a given color c at the chemical potential μ is

$$N_c(\mu) = \int_{E_{\min}}^{\mu} dE \bar{\rho}_c(E), \quad (19)$$

where E_{\min} is the minimum energy in the spectrum. The maximum value of $N_c(\mu)$ is $N_{c,\max} = q$, since there is maximum of one color state c per site, and q is the number of sites contained in the real space magnetic unit cell. The filling factor for color c is defined as the ratio

$$\nu_c(\mu) = \frac{N_c(\mu)}{N_{c,\max}}, \quad (20)$$

which has a maximal value of one, that is, $\nu_{c,\max} = 1$.

The total density of states within the magnetic unit cell can be written as

$$\bar{\rho}(E) = \sum_c \bar{\rho}_c(E), \quad (21)$$

while the total density of states per site has the form

$$\rho(E) = \frac{\bar{\rho}(E)}{q}. \quad (22)$$

The total density of states $\bar{\rho}(E)$, within the unit cell, integrates to $3q$ states over all energies, while the density of states per site $\rho(E)$ always integrates to 3, because we

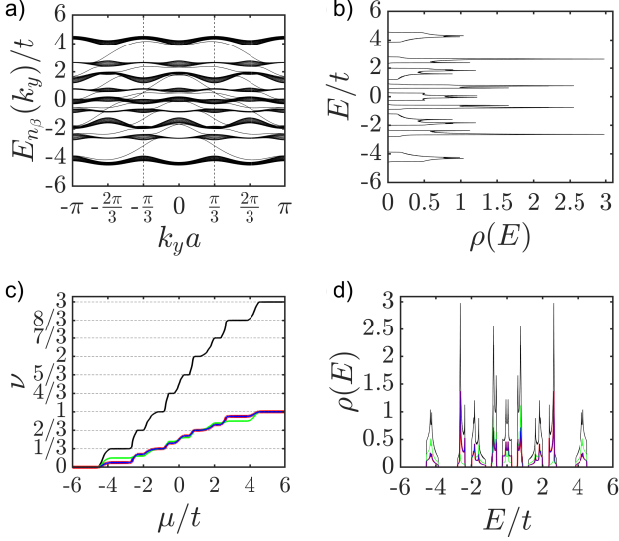


FIG. 4. (Color Online) Spectroscopic properties and filling factor for parameters $\alpha = 1/3$, $k_T a = \pi/8$ and $h_x/t = 1.85$. This corresponds to a vertical line across the phase diagram of Fig. 2b. a) Energy spectrum $E_{n_\beta}(k_y)/t$ versus $k_y a$ for the case of open boundary conditions, showing explicitly midgap edge states. The panels b), c) and d) refer to the case of periodic boundary conditions. b) Energy E/t versus total density of states per site $\rho(E)$ to illustrate the gaps between the bands, which coincide with the gaps for the case of open boundary conditions. c) Filling factor ν versus chemical potential μ/t showing steps where incompressible insulating phases occur. d) Density of states per site $\rho(E)$ versus energy E/t . The total color density states per site $\rho(E)$ is in black, and the color density of states are in red for the Red (R) states, in green for the Green (G) states and in blue for the Blue (B) states.

have a maximum of three colors per site. The total filling factor at chemical potential μ is

$$\nu(\mu) = \sum_c \nu_c(\mu), \quad (23)$$

having a maximum value $\nu_{\max} = 3$.

In Fig. 4, we show spectroscopic information for particular values of parameters: the magnetic flux ratio $\alpha = 1/3$, the color-flip field $h_x/t = 1.85$ and the color-orbit coupling parameter $k_T a = \pi/8$. All these parameters are the same for Figs. 4a through 4d. The choice of these parameters illustrates a vertical scan at $h_x/t = 1.85$ in Fig. 2b. The vertical line cuts through a wide variety of topological phases as the chemical potential μ grows.

In Fig. 4a, we show the energy eigenspectrum versus momentum $k_y a$ for open boundary conditions, where eight gaps can be seen in the spectrum corresponding to the insulating phases of the vertical scan in Fig. 2b at $h_x/t = 1.85$. The energy dispersions of the midgap edge states are also shown. The first gap ($r = 1$) corresponds to the red region in Fig. 2b with one chiral midgap edge state with positive chirality and topological numbers $(S_1, C_1) = (0, +1)$. The second gap ($r = 2$) corresponds

to the blue region in Fig. 2b with two chiral midgap edge states with positive chirality and topological numbers $(S_2, C_2) = (0, +2)$. The third gap ($r = 3$) corresponds to the orange region in Fig. 2b with two chiral midgap edge states with opposite chirality and topological numbers $(S_3, C_3) = (+1, 0)$. The fourth gap ($r = 4$) corresponds to the red-with-black-dots region in Fig. 2b with two chiral midgap edge states with positive chirality, one chiral midgap state with negative chirality and topological numbers $(S_4, C_4) = (+1, +1)$. The fifth gap ($r = 5$) corresponds to the yellow-with-black-dots region in Fig. 2b with two chiral midgap edge states with negative chirality, one chiral midgap state with positive chirality and topological numbers $(S_5, C_5) = (+2, -1)$. The sixth gap ($r = 6$) corresponds to the orange region in Fig. 2b with two chiral midgap edge states with opposite chirality and topological numbers $(S_6, C_6) = (+2, 0)$. The seventh gap ($r = 7$) corresponds to the green region in Fig. 2b with two chiral midgap edge states with negative chirality and topological numbers $(S_7, C_7) = (+3, -2)$. The eighth gap ($r = 8$) corresponds to the yellow region in Fig. 2b with one chiral midgap edge state with negative chirality and topological numbers $(S_8, C_8) = (+3, -1)$.

In Fig. 4b, we show a plot of energy E versus total color density of states per site $\rho(E)$ for periodic boundary conditions to indicate explicitly the location of the gaps in the energy spectrum. We used a small imaginary part ($\delta = 5 \times 10^{-3}t$) to calculate $\rho(E)$ from $G_{cc}(z = E + i\delta)$. The eight energy gaps can be clearly seen at the locations where the total color density of states in the bulk is zero. The regions associated with these gaps correspond to the eight phases that are crossed in a vertical scan in Fig. 2b at $h_x/t = 1.85$ as the chemical potential μ or filling factor ν grows.

In Fig. 4c, we show a plot of the color filling factors ν_c and the total filling factor ν versus chemical potential μ , calculated using the color density of states per site $\rho_c(E)$ and the total color density of states per site $\rho(E)$, respectively. Notice that when the chemical potential μ lies inside a band gap, the filling factor ν is constant and take the exact form $\nu = r/q$ as discussed in connection to the gap labelling theorem of Sec. VB. The gapped phases (the chemical potential μ lies inside of a gap) are incompressible, because the total color filling factor ν and the color filling factor ν_c for each color is constant, and the color compressibility κ_c is proportional to $d\nu_c(\mu)/d\mu = 0$. Naturally, the sequence of insulating phases crossed as μ increases is exactly the same as that in Fig. 2b. At $\nu = 0$ and $\nu = 3$, we have trivial insulating phases. At $\nu = 1/3$, there is a red region with topological quantum numbers $(S_1, C_1) = (0, +1)$. At $\nu = 2/3$, there is a blue region with topological quantum numbers $(S_2, C_2) = (0, +2)$. At $\nu = 1$, there is an orange region with topological quantum numbers $(S_3, C_3) = (+1, 0)$. At $\nu = 4/3$, there is a red-with-black-dots region with topological quantum numbers $(S_4, C_4) = (+1, +1)$. At $\nu = 5/3$, there is a yellow-with-black-dots region with topological quantum numbers $(S_5, C_5) = (+2, -1)$. At

$\nu = 2$, there is an orange region with topological quantum numbers $(S_6, C_6) = (+2, 0)$. At $\nu = 7/3$, there is a green region with topological quantum numbers $(S_7, C_7) = (+3, -2)$. At $\nu = 8/3$, there is a yellow region with topological quantum numbers $(S_1, C_1) = (+3, -1)$. Notice also that filling factors $\nu_R = \nu_B$ reflecting a symmetry of the Hamiltonian operator in Eq. (1) via the simultaneous exchange $R \leftrightarrow B$ and $k_T \leftrightarrow -k_T$.

In Fig. 4d, we show a plot of the color density of states per site ρ_c and the total color density of states per site ρ versus energy E . Notice that $\rho_R(E) = \rho_B(E)$, reflecting a symmetry of the Hamiltonian operator in Eq. (1) via the simultaneous exchange $R \leftrightarrow B$ and $k_T \leftrightarrow -k_T$. One can clearly see the eight bands characterizing the insulating states discussed in Fig. 4c. The total color density states per site $\rho(E)$ is in black, and the color density of states are in red for the Red (R) states, in green for the Green (G) states and in blue for the Blue (B) states.

VII. SUMMARY AND CONCLUSIONS

We investigated the eigenspectrum, Chern numbers and phase diagrams of ultracold color-orbit coupled SU(3) fermions in optical lattices, having in mind possible experimental systems, such as fermionic isotopes ^{137}Yb and ^{87}Sr . We labeled the internal states of the atoms by colors Red (R), Green (G) and Blue (B), and analyzed the quantum phases as a function of artificial magnetic, color-orbit and color-flip fields that can be independently controlled.

For fixed artificial magnetic flux ratio, we identified topological quantum phases and phase transitions in the phase diagrams of chemical potential versus color-flip fields or color-orbit coupling, where the chirality and number of midgap edge states change. We established a gap labelling theorem to characterize the insulating

phases by their filling factors and topological quantum numbers.

The topologically non-trivial phases are classified in three groups: the first group has total non-zero chirality and exhibit only the quantum charge Hall effect; the second group has total non-zero chirality and exhibit both quantum charge and quantum color Hall effects; and the third group has total zero chirality, but exhibit the quantum color Hall effect. These phases are generalizations of the quantum Hall and quantum spin Hall phases for charged spin-1/2 fermions.

Lastly, we described the color density of states per site and a staircase structure in the total and color filling factors versus chemical potential for fixed color-orbit, color-flip and magnetic flux ratio. We showed the existence of incompressible states at rational filling factors precisely given by a gap labelling theorem that related the filling factors to the magnetic flux ratio and topological quantum numbers.

Our theoretical findings pave the way for the experimental discovery of topological insulating phases that present simultaneously a quantum charge Hall effect (QChH) and a quantum color Hall effect (QCoH) in SU(3) fermions such as ^{173}Yb or ^{87}Sr . This particular phase has no correspondence for spin-1/2 fermions in condensed matter or ultracold atomic physics, where the quantum Hall and the quantum spin Hall phases are mutually exclusive.

ACKNOWLEDGMENTS

One of us (C.A.R.S.d.M.) would like to thank the support of the Galileo Galilei Institute for Theoretical Physics (Florence, Italy) via a Simons Fellowship, and of the International Institute of Physics (Natal, Brazil) via its Visitor's Program.

-
- [1] Takeshi Fukuhara, Yosuke Takasu, Mitsutaka Kumakura and Yoshiro Takahashi, Degenerate Fermi Gases of Ytterbium, *Phys. Rev. Lett.* **98**, 030401 (2007).
 - [2] M. A. Cazalilla, A. F. Ho and M. Ueda, Ultracold Gases of Ytterbium: Ferromagnetism and Mott states in an SU(6) Fermi System, *New. J. Phys.* **11**, 103033 (2009).
 - [3] Shintaro Taie, Yosuke Takasu, Seiji Sugawa, Rekishu Yamazaki, Takuya Tsujimoto, Ryo Murakami and Yoshiro Takahashi, Realization of a SU(2) \times SU(6) System of Fermions in a Cold Atomic Gas, *Phys. Rev. Lett.* **105**, 190401 (2010).
 - [4] Shintaro Taie, Rekishu Yamazaki, Seiji Sugawa and Yoshiro Takahashi, An SU(6) Mott Insulator of an Atomic Fermi Gas Realized by Large-spin Pomeranchuk Cooling, *Nat. Phys.* **8**, 825-830 (2012).
 - [5] Guido Pagano, Marco Mancini, Giacomo Cappellini, Pietro Lombardi, Florian Schäfer, Hui Hu, Xia-Ji Liu, Jacopo Catani, Carlo Sias, Massimo Inguscio and Leonardo Fallani, A One-dimensional Liquid of Fermions with Tunable Spin, *Nat. Phys.* **10**, 198-201 (2014).
 - [6] Christian Hofrichter, Luis Riegger, Francesco Scazza, Moritz Höfer, Diogo Rio Fernandes, Immanuel Bloch, and Simon Fölling, Direct Probing of the Mott Crossover in the SU(N) Fermi-Hubbard Model, *Phys. Rev. X* **6**, 021030 (2016).
 - [7] B. J. DeSalvo, M. Yan, P. G. Mickelson, Y. N. Martinez de Escobar, and T. C. Killian, Degenerate Fermi Gas of ^{87}Sr , *Phys. Rev. Lett.* **105**, 030402 (2010).
 - [8] Meng Khoon Tey, Simon Stellmer, Rudolf Grimm and Florian Schreck, Double-degenerate Bose-Fermi Mixture of Strontium, *Phys. Rev. A* **82**, 011608(R) (2010).
 - [9] Simon Stellmer, Rudolf Grimm and Florian Schreck, Detection and Manipulation of Nuclear Spin States in Fermionic Strontium, *Phys. Rev. A* **84**, 043611 (2011).
 - [10] Simon Stellmer, Florian Schreck and Thomas C. Killian, Degenerate Quantum Gases of Strontium, *arXiv:1307.0601* (2013).
 - [11] Simon Stellmer, Florian Schreck and Thomas C. Killian,

- Chapter 1: Degenerate Quantum Gases of Strontium, Annual Review of Cold Atoms and Molecules, pp 1-80, World Scientific (2014).
- [12] G. Pagano, M. Mancini, G. Cappellini, L. Livi, C. Sias, J. Catani, M. Inguscio, and L. Fallani, Strongly Interacting Gas of Two-Electron Fermions at an Orbital Feshbach Resonance, *Phys. Rev. Lett.* **115**, 265301 (2015).
- [13] M. Höfer, L. Riegger, F. Scazza, C. Hofrichter, D. R. Fernandes, M. M. Parish, J. Levinsen, I. Bloch and S. Fölling, Observation of an Orbital Interaction-Induced Feshbach Resonance in ^{173}Yb , *Phys. Rev. Lett.* **115**, 265302 (2015).
- [14] Y.-J. Lin, R. L. Compton, K. Jiménez-García, J. V. Porto and I. B. Spielman, Synthetic Magnetic Fields for Ultracold Neutral Atoms, *Nature* **462**, 628 (2009).
- [15] M. Aidelsburger, M. Atala, M. Lohse, J. T. Barreiro, B. Paredes, and I. Bloch, Realization of the Hofstadter Hamiltonian with Ultracold Atoms in Optical Lattices, *Phys. Rev. Lett.* **111**, 185301 (2013).
- [16] Hirokazu Miyake, Georgios A. Siviloglou, Colin J. Kennedy, William Cody Burton, and Wolfgang Ketterle, Realizing the Harper Hamiltonian with Laser-Assisted Tunneling in Optical Lattices *Phys. Rev. Lett.* **111**, 185302 (2013).
- [17] K. von Klitzing, G. Dorda, and M. Pepper, New Method for High-Accuracy Determination of the Fine-Structure Constant Based on Quantized Hall Resistance, *Phys. Rev. Lett.* **45**, 494 (1980).
- [18] D. C. Tsui, H. L. Stormer, and A. C. Gossard, Two-Dimensional Magnetotransport in the Extreme Quantum Limit, *Phys. Rev. Lett.* **48**, 1559 (1982).
- [19] P. G. Harper, Single Band Motion of Conduction Electrons in a Uniform Magnetic Field, *Proc. Phys. Soc. London Sect. A* **68**, 874 (1955).
- [20] D. R. Hofstadter, Energy levels and wave functions of Bloch electrons in rational and irrational magnetic fields, *Physical Review B* **14**, 2239-2249 (1976).
- [21] M. Aidelsburger, M. Lohse, C. Schweizer, M. Atala, J. T. Barreiro, S. Nascimbène, N. R. Cooper, I. Bloch and N. Goldman, Measuring the Chern Number of Hofstadter Bands with Ultracold Bosonic Atoms, *Nature Phys.* **11**, 162 (2015).
- [22] N. Dupuis, G. Montambaux, and C. A. R. Sá de Melo, Quasi-one-dimensional Superconductors in Strong Magnetic Fields, *Phys. Rev. Lett.* **70**, 2613 (1993).
- [23] G. Montambaux, N. Dupuis and C. A. R. Sá de Melo, Quasi-one-dimensional Superconductors in Strong Magnetic Field, *Physica B* 194-196, 1383 (1994).
- [24] C. A. R. Sá de Melo, Paramagnetism and Reentrant Behavior in Quasi-one-dimensional Superconductors at High Magnetic Fields, *Physica C* **260**, 224 (1996).
- [25] C. A. R. Sá de Melo, Singlet versus Triplet Superconductivity in Quasi-one-dimensional Systems: Magnetic Field Effects, "The Superconducting State in Magnetic Fields: Special Topics and New Trends", pp. 296-324, World Scientific, Singapore (1998).
- [26] Y. -J. Lin, K. Jiménez-García, and I. B. Spielman, Spin-orbit Coupled Bose-Einstein Condensates, *Nature (London)* **471**, 83 (2011).
- [27] C. L. Kane and E. J. Mele, Z_2 Topological Order and the Quantum Spin Hall Effect, *Phys. Rev. Lett.* **95**, 146802 (2005).
- [28] L. Sheng, D. N. Sheng, C. S. Ting, and F. D. M. Haldane, Nondissipative Spin Hall Effect via Quantized Edge Transport, *Phys. Rev. Lett.* **95**, 136602 (2005).
- [29] B. A. Bernevig and S.-C. Zhang, Quantum Spin Hall Effect, *Phys. Rev. Lett.* **96**, 106802 (2006).
- [30] N. Fläschner, B. S. Rem, M. Tarnowski, D. Vogel, D.-S. Lühmann, K. Sengstock and C. Weitenberg, Experimental Reconstruction of the Berry Curvature in a Floquet Bloch Band, *Science* **352**, 1091 (2016).
- [31] E. Zhao, N. Bray-Ali, C. J. Williams, I. B. Spielman, and I. I. Satija, Chern Numbers Hiding in Time-of-flight Images, *Phys. Rev. A* **84**, 063629 (2011).
- [32] P. Hauke, M. Lewenstein and A. Eckardt, Tomography of Band Insulators from Quench Dynamics, *Phys. Rev. Lett.* **113**, 045303 (2014).
- [33] G. Jotzu, M. Messer, R. Desbuquois, M. Lebrat, T. Uehlinger, D. Greif and T. Esslinger, Experimental Realization of the Topological Haldane Model with Ultracold Fermions, *Nature* **515**, 237 (2014).
- [34] H. M. Price, and N. R. Cooper, Mapping the Berry curvature from Semiclassical Dynamics in Optical Lattices, *Phys. Rev. A* **85**, 033620 (2012).
- [35] A. Dauphin, N. Goldman, Extracting the Chern Number from the Dynamics of a Fermi Gas: Implementing a Quantum Hall Bar for Cold Atoms, *Phys. Rev. Lett.* **111**, 135302 (2013).
- [36] W. Beugeling, N. Goldman, and C. Morais Smith, Topological Phases in a Two-dimensional lattice: Magnetic Field versus Spin-orbit Coupling, *Phys. Rev. B* **86**, 075118 (2012).
- [37] Man Hon Yau and C. A. R. Sá de Melo, Chern-number Spectrum of Ultracold Fermions in Optical Lattices Tuned Independently via Artificial Magnetic, Zeeman, and Spin-orbit fields, *Phys. Rev. A* **99**, 043625 (2019).
- [38] N. Goldman, I. Satija, P. Nikolic, A. Bermudez, M. A. Martin-Delgado, M. Lewenstein, and I. B. Spielman, Realistic Time-Reversal Invariant Topological Insulators with Neutral Atoms, *Phys. Rev. Lett.* **105**, 255302 (2010).
- [39] Di Lao, Chandra Raman, and C. A. R. Sá de Melo, Nematic-Orbit Coupling and Nematic Density Waves in Spin-1 Condensates, *Phys. Rev. Lett.* **124**, 173203 (2020).
- [40] D. M. Kurkcuoglu and C. A. R. Sá de Melo, Creating Spin-one Fermions in the Presence of Artificial Spin-orbit Fields: Emergent Spinor Physics and Spectroscopic Properties, *J. Low. Temp. Phys.* **191**, 174 (2018).
- [41] D. M. Kurkcuoglu and C. A. R. Sá de Melo, Color Superfluidity of Neutral Ultracold Fermions in the Presence of Color-flip and Color-orbit fields, *Phys. Rev. A* **97**, 023632 (2018).
- [42] N. Goldman, J. Dalibard, A. Dauphin, F. Gerbier, M. Lewenstein, P. Zoller, I. B. Spielman, Direct Imaging of Topological Edge States in Cold-atom Systems, *Proc. Natl. Acad. Sci. U.S.A.* **110**, 6736 (2013).
- [43] D. J. Thouless, M. Kohmoto, M. P. Nightingale, and M. den Nijs, Quantized Hall Conductance in a Two-Dimensional Periodic Potential, *Phys. Rev. Lett.* **49**, 405-408 (1982).
- [44] M. Kohmoto, Topological Invariant and the Quantization of the Hall Conductance, *Ann. Phys.* **160**, 343-354 (1985).
- [45] T. Fukui, Y. Hatsugai and H. Suzuki, Chern Numbers in Discretized Brillouin Zone: Efficient Method of Computing (Spin) Hall Conductances, *J. Phys. Soc. Jpn.* **74**, 1674 (2005).

- [46] Y. Hatsugai, Topological Aspects of the Quantum Hall Effect, J. Phys.: Condens. Matter **9**, 2507 (1997).
- [47] G. H. Wannier, A Result Not Dependent on Rationality for Bloch Electrons in a Magnetic Field, Phys. Stat. Sol. (b) **88**, 757-765 (1978).
- [48] F. H. Claro and G. H. Wannier, Magnetic Subband Structure of Electrons in Hexagonal Lattices, Phys. Rev. B **19**, 6068 (1979).